# Investigation of thermal radiation effects on solid oxide fuel cell performance by a comprehensive model

Min Zeng [a,b], Jinliang Yuan [b], Jian Zhang [a], Bengt Sundén [b], Qiuwang Wang [a,*]

[a] Key Laboratory of Thermo-Fluid Science and Engineering, MOE, Xi'an Jiaotong University, Xi'an, Shaanxi 710049, China
[b] Department of Energy Sciences, Faculty of Engineering, Lund University, P.O. Box 118, SE-222 100 Lund, Sweden

## ABSTRACT

Thermal radiation in the air and fuel channels has the potential to dramatically influence the overall operating conditions and performance of solid oxide fuel cells. A 3D comprehensive model is developed, with emphasis on quantifying the radiative heat transfer process and its effects. The radiosity method is used for the thermal radiation in the air and fuel channels. The thermal radiation heat transfer is coupled to the overall energy conservation equation. Commercially available COMSOL CFD software is used as a platform for the global thermal-fluid modeling of the SOFC. The effects of the operating voltage, emissivity, ambient temperature and flow arrangement (Co- and Counter-flow) on the performance of SOFC are investigated. The predicted results reveal that the radiative heat transfer should be considered in SOFC modeling simulation, and the effects of the thermal radiation on the performance of SOFC under a different flow arrangement is sometimes quite significant.

© 2012 Elsevier B.V. All rights reserved.

## 1. Introduction

Solid oxide fuel cells (SOFCs) are promising energy sources that are very attractive due to their high energetic efficiency and low emission of pollutants from the exhaust gases into the environment. However, the SOFCs have their drawbacks. There are thermal expansion mismatches among multifunctional materials due to the high operating temperature (up to 1200 K) [1]. Therefore it is of major importance to predict accurately the temperature field within the cells in order to detect the hot spots and the maximum thermal gradients [2]. Due to the high operating temperature, radiative heat transfer must be given special consideration in any modeling and design efforts, including stack thermal management and materials development. In SOFCs, the radiative heat transfer usually consists of three parts: the surface-to-surface heat exchange in anode and cathode channels; the thermal radiation of participating media in the reactants and products; the thermal radiation of translucent electrolyte and electrode layers. During the last decades, many researchers have paid attention to investigations of the radiative heat transfer coupled with electro-chemical and transport processes in SOFCs [3–15].

In references [3–5], the authors regarded the radiative heat transfer to have a great effect on the heat transfer rate in SOFCs. Damm and Fedorov [6,7] investigated the effects of radiative heat

transfer in the electrode and the electrolyte layers. Their results revealed that the electrodes can be regarded as optical transparent material, and the radiative heat transfer within the electrodes had a negligible effect on the average cell operating temperature, voltage, or temperature gradients. However, the effects of radiation heat transfer within the electrolyte depend on the thickness of electrolyte layer, i.e., the thicker the electrolyte layer, the greater the impact of radiative heat transfer. The radiative heat transfer had little influence when the thickness of the electrolyte was less than 15 $\mu$m. The same conclusion was drawn by Daun et al. [8]. The radiative heat transfer with the participating media in SOFCs was investigated in detail by Vandersteen and Pharoah [9]. Because of the low emissivity of the gas and the small channel sizes, the gas was optically thin, and the effect of participating media on thermal radiation was minimal in the planar geometry, but it was likely to be significant in the tubular geometry. Sanchez et al. [10] also investigated the radiative heat transfer with participating media in the anode and they found it had little influence on the performance of SOFCs under the ordinary operation conditions. They also indicated that the surface-to-surface thermal radiation in the flow channels had great effects on the SOFCs. Yakabe et al. [11] numerically investigated the effects of surface-to-surface thermal radiation on the performance of planar SOFCs, and revealed that the temperature distribution in the cell became flat as the radiative heat exchange inside the channels was considered.

The radiative heat transfer has received much more attention in recent years [2,12–14]. Based on a Monte Carlo Ray Tracing method, a numerical methodology aimed to predict the thermal radiation of

* Corresponding author. Tel.: +86 29 82663222; fax: +86 29 82663502.
*E-mail address:* wangqw@mail.xjtu.edu.cn (Q. Wang).

## Nomenclature

| | |
|---|---|
| $A_v$ | relative surface area per unit volume ($m^2\, m^{-3}$) |
| $c$ | concentration of species ($mole\, m^{-3}$) |
| $c_p$ | specific heat ($J\, kg^{-1}\, K^{-1}$) |
| $d$ | pore diameter (m) |
| $D_{ij}^{eff}$ | effective diffusion coefficient ($m^2\, s$) |
| $F$ | view factor |
| $G$ | irradiation ($W\, m^{-2}$) |
| $h$ | convective heat transfer coefficient ($W\, m^{-2}\, K^{-1}$) |
| $H$ | channel height or layer thickness (m) |
| $i$ | current density ($A\, m^{-2}$) |
| $J$ | radiosity ($W\, m^{-2}$); kinetically controlled local current density ($A\, m^{-3}$) |
| $L$ | cell length (m) |
| $m$ | molar flow rate ($mol\, s^{-1}$) |
| $n$ | number fraction of particles |
| $p$ | pressure (Pa); probability of percolation in reaction zone |
| $q_r$ | net heat transfer rate from a surface ($W\, m^{-2}$) |
| $r$ | radius of electron-conduction particles (m) |
| $T$ | temperature (K) |
| $\mathbf{u}$ | velocity vector ($m\, s^{-1}$) |
| $W$ | flow channel width (m) |
| $x$ | molar fraction |

*Greek*

| | |
|---|---|
| $\varepsilon$ | porosity;emissivity |
| $\eta$ | overpotential (V) |
| $\theta$ | contact angle between electron- and ion- conducting particles in reaction zone (°) |
| $\kappa$ | permeability ($m^2$) |
| $\lambda$ | thermal conductivity ($W\, m^{-1}\, K^{-1}$) |
| $\sigma$ | electrical/ionic conductivity ($S\, m^{-1}$); Stefan–Boltzmann constant ($5.67 \times 10^{-8}\, W\, m^{-2}\, K^{-4}$) |
| $\tau$ | tortuosity |
| $\varphi$ | potential (V) |
| $\Phi$ | volume fraction |
| $\omega_i$ | mass fraction of species $i$ |

*Subscripts*

| | |
|---|---|
| amb | ambient |
| ASL | anode support layer |
| ARL | anode reaction layer |
| CRL | cathode reaction layer |
| E | electrolyte |
| CDL | cathode diffusion layer |
| el | electronic |
| io | ionic |

*Superscrits*

| | |
|---|---|
| eff | effective |

materials used in the cell design with a planar geometry was developed in [2]. Kee et al. [12] developed a relatively simple model to rapidly evaluate various configurations and operating conditions for tubular anode-supported SOFC stacks, and they concluded that the radiative heat transfer is remarkably effective at removing the heat from tube bundles of the stack. A surface-to-surface radiation model was employed in [13] to analyse the influence of different operating conditions on the temperature distribution in the anode-supported tubular cell. A mathematical evaluation of view factors for radiative heat exchange in longitudinally distributed SOFC

**Table 1**
Geometry of unit cell.

| Geometry | Value | Reference |
|---|---|---|
| Cell length $L$ (m) | $2.0 \times 10^{-2}$ | / |
| Flow channel width $W_{CH}$ (m) | $1.0 \times 10^{-3}$ | [17] |
| Flow channel height $H_{CH}$ (m) | $1.0 \times 10^{-3}$ | [17] |
| Anode support layer thickness $H_{ASL}$ (m) | $1.0 \times 10^{-3}$ | [16,17] |
| Anode reaction layer thickness $H_{ARL}$ (m) | $2.0 \times 10^{-5}$ | [16,17] |
| Electrolyte thickness $H_E$ (m) | $8.0 \times 10^{-6}$ | [16,17] |
| Cathode reaction layer thickness $H_{CRL}$ (m) | $2.5 \times 10^{-5}$ | [16,17] |
| Cathode diffusion layer thickness $H_{CDL}$ (m) | $1.3 \times 10^{-5}$ | [16,17] |

modeling was introduced by Bao et al. [14]. The detailed radiation model based on analytical view factors predicted more uniform distribution of the cell temperature and current density in the overall SOFC modeling. Nevertheless, most of the existing heat transfer models for the SOFCs simply ignored the effect of thermal radiation [15], even though this effect is important when the cell operating temperature is higher than 800 K [4]. As some authors argued, the view factor, depending on the cell geometry and configuration, has a great influence on the surface-to-surface radiation exchange. However, 2D models, available in most existing studies [4,8,10,12,15], could not account for this phenomenon.

By considering various configurations of interconnect, fuel channel, anode support layer, anode reaction layer, electrolyte, cathode reaction layer, cathode diffusion layer and air channel, a 3D fuel cell unit model is developed, and implemented in the software COMSOL to verify if radiative heat transfer is really an important phenomenon in flow channels of the typical planar SOFCs. Next, we validate the model with some experimental data. Finally, with the validated model, we investigate the effects of emissivity, ambient temperature and flow configuration on the SOFC performance.

## 2. Physical model and computational method

### 2.1. Physical model

In general, one cell-stack is constructed consisting of repeated single unit cells. Fig. 1(a) shows a schematic diagram of single cell composed of five pairs of parallel gas flow channels. Since much more time is needed to simulate the cell performance for the whole stack, a simplified single-unit cell with all the components is selected in the present work. Fig. 1(b) and (c) shows the repeated unit cell located in the middle part of the stack. For validation of the present model, the configuration and the parameters are chosen based on the experimental work by Jung et al. [16]. The detailed geometry, operating parameters and properties are listed in Tables 1–3, separately.

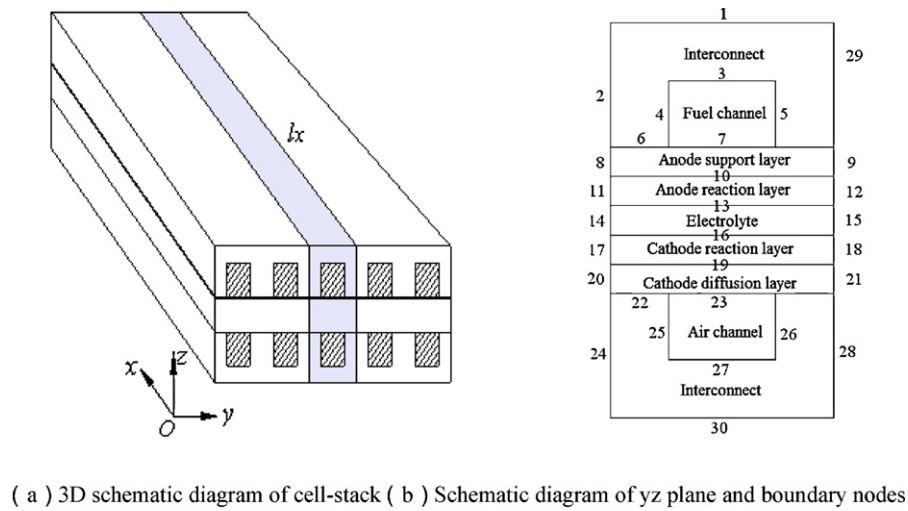### 2.2. Mathematical formulations and computational method

#### 2.2.1. Thermal radiation model

Inclusion of radiative heat transfer in the analysis of the cell performance includes a number of challenges, particularly as the

**Table 2**
Baseline conditions.

| Variable | Value | Reference |
|---|---|---|
| Operating temperature $T$ (K) | 1073 | [16,17] |
| Operating pressure $p$ (Pa) | $1.013 \times 10^5$ | [16,17] |
| Anode gas inlet molar flow rate $m_{AI}$ ($mol\, s^{-1}$) | $5.68 \times 10^{-5}$ | [17] |
| Cathode gas inlet molar flow rate $m_{CI}$ ($mol\, s^{-1}$) | $1.48 \times 10^{-4}$ | [17] |
| Inlet molar fraction of $H_2$ at anode $x_{H_2 I}$ | 0.97 | [16,17] |
| Inlet molar fraction of $H_2O$ at anode $x_{H_2O I}$ | 0.03 | [16,17] |
| Inlet molar fraction of $O_2$ at cathode $x_{O_2 I}$ | 0.21 | [16,17] |
| Inlet molar fraction of $N_2$ at cathode $x_{N_2 I}$ | 0.79 | [16,17] |

( a ) 3D schematic diagram of cell-stack ( b ) Schematic diagram of yz plane and boundary nodes



( c ) Schematic diagram of xz plane

**Fig. 1.** Computational domain.

thermal radiation is coupled with analysis of convective–conductive heat transfer [7,21]. The first is the inherent complexity of the radiation governing equations, which are integral-differential equations and, in general, depend on as many as seven independent variables (time, three position variables, two angular variables describing direction of propagation of radiation rays, and the wavelength). Furthermore, the governing equations are non-linear, as the emissive power features a fourth-power dependence on the temperature. Besides the difficulty associated with solving these equations, the accuracy of any analysis is always limited by the extent to which radiative properties are known [7]. Many researchers tried to use different methods to model the radiation heat transfer, such as the Monte Carlo method [2,8,9], Schuster–Schwartchild two-flux approximation method [4,6,8], and Hottel zone method [5]. To make a simple radiation analysis possible, all the surfaces in the channels are assumed to be opaque, diffuse and gray in this study. The radiosity method is introduced to determine the net radiation heat transfer rate of the surfaces. This method includes the concepts of radiostiy and irradiation, etc.

The radiosity represents the rate at which radiation energy leaves a unit area of a surface in all directions [21]. For an opaque surface, the radiosity can be expressed as

$$J = (1 - \varepsilon)G + \varepsilon\sigma T^4 \tag{1}$$

where $J$ is the radiosity (W m$^{-2}$); $\varepsilon$ is the surface emissivity; $G$ is the irradiation (W m$^{-2}$); $\sigma$ is the Stefan–Boltzmann constant ($5.67 \times 10^{-8}$ W m$^{-2}$ K$^{-4}$).

The radiation flux incident on a surface from all directions is called irradiation $G$, and is expressed as [21]

$$G = G_\text{m} + F_\text{amb}\sigma T_\text{amb}^4 \tag{2}$$

where $G_\text{m}$ is the mutual irradiation, coming from other surfaces in the model (W m$^{-2}$); $F_\text{amb}$ is the ambient view factor; $T_\text{amb}$ is the ambient temperature (K).

For the specific point, $\mathbf{m}(x, y, z)$, in a surface, the irradiation of the point $\mathbf{m}'$ $(x', y', z')$ to the point $\mathbf{m}(x, y, z)$ can be defined as

$$G_\text{m} = \int_{S'} \frac{(-\boldsymbol{n}' \cdot \boldsymbol{r})(\boldsymbol{n} \cdot \boldsymbol{r})}{\pi|\boldsymbol{r}|^4}J'dS \tag{3}$$

where $S$ is the wall surface area (m$^2$); $\mathbf{n}'$ is the unit normal factor of $\mathbf{m}'$ $(x', y', z')$ in solid surface. $\mathbf{r}$ is the vector from the point $\mathbf{m}(x, y, z)$ to $\mathbf{m}'$ $(x', y', z')$; $\mathbf{n}$ is the unit normal factor of $\mathbf{m}(x, y, z)$ in solid surface; $J'$ is the radiosity of $\mathbf{m}'$ $(x', y', z')$.

In Eq. (2), the ambient view factor is evaluated by

$$F_\text{amb} = 1 - \int_{S'} \frac{(-\mathbf{n}' \cdot r)(\mathbf{n} \cdot r)}{\pi|\mathbf{r}|^4}dS \tag{4}$$

According to the energy balance, the net flux of the heat transfer from a surface is denoted by $q_r$ and is expressed as

$$q_r = J - G \tag{5}$$

With Eqs. (1), (2) and (5), the net radiation heat transfer rate can be acquired.

### 2.2.2. Governing equations and boundary conditions

Transport phenomena in SOFCs contain momentum, mass, electron, ion and heat transfer, which are coupled with each other. Due to the multiphysics nature of SOFCs, various governing equations (except for continuity equation) and boundary conditions are outlined separately in the following sections.

**Table 3**
Properties of material.

| Variable | Value | Reference |
|---|---|---|
| Porosity of anode support layer $\varepsilon_{ASL}$ | 0.42 | [16,17] |
| Porosity of anode reaction layer $\varepsilon_{ARL}$ | 0.097 | [16,17] |
| Porosity of cathode support layer $\varepsilon_{CRL}$ | 0.40 | [17] |
| Porosity of cathode diffusion layer $\varepsilon_{CDL}$ | 0.36 | [16,17] |
| Average pore diameter of anode support layer $d_{ASL}$ ($\mu$m) | 1.40 | [16,17] |
| Average pore diameter of anode reaction layer $d_{ARL}$/($\mu$m) | 0.33 | [16,17] |
| Average pore diameter of cathode reaction layer $d_{CRL}$ ($\mu$m) | 2.00 | [16,17] |
| Average pore diameter of cathode diffusion layer $d_{CDL}$($\mu$m) | 1.40 | [16,17] |
| Tortuosity of anode support layer $\tau_{tort,ASL}$ | 3 | [17] |
| Tortuosity of anode reaction layer $\tau_{tort,ARL}$ | 3 | [17] |
| Tortuosity of cathode reaction layer $\tau_{tort,CRL}$ | 3 | [17] |
| Tortuosity of cathode diffusion layer $\tau_{tort,CDL}$ | 3 | [17] |
| Permeability of anode support layer $\kappa_{ASL}$ (m$^2$) | $3.4 \times 10^{-14}$ | [16,17] |
| Permeability of anode reaction layer $\kappa_{ARL}$ (m$^2$) | $3.4 \times 10^{-14}$ | [17] |
| Permeability of cathode reaction layer $\kappa_{CRL}$ (m$^2$) | $5.4 \times 10^{-14}$ | [16,17] |
| Permeability of cathode diffusion layer $\kappa_{CDL}$/m$^2$ | $3.7 \times 10^{-14}$ | [16,17] |
| Volume fraction of electron-conducting particles (Ni) in anode support layer $\Phi_{elASL}$ | 0.4 | [17] |
| Volume fraction of electron-conducting particles (Ni) in anode reaction layer $\Phi_{elARL}$ | 0.4 | [17] |
| Volume fraction of electron-conducting particles (LSM-YSZ) in cathode reaction layer $\Phi_{elCRL}$ | 0.587 | [17] |
| Volume fraction of electron-conducting particles (LSM) in cathode diffusion layer $\Phi_{elCDL}$ | 1.0 | [17] |
| Electrical conductivity of anode support layer $\sigma_{elASL}$ (S m$^{-1}$) | $1.011 \times 10^5$ | [16,17] |
| Electrical conductivity of anode reaction layer $\sigma_{elARL}$(S m$^{-1}$) | $1.011 \times 10^5$ | [16,17] |
| Ionic conductivity of anode reaction layer $\sigma_{ioARL}$ (S m$^{-1}$) | $(1 - \Phi_{ARL}) \left( \dfrac{1 - \varepsilon_{ARL}}{\tau_{tort,ARL}} \right) \sigma_{ioEL}$ | [18] |
| Ionic conductivity of electrolyte layer $\sigma_{ioE}$ (S m$^{-1}$) | $3.34 \times 10^4 \exp \left( \dfrac{-10300}{T} \right)$ | [19] |
| Ionic conductivity of cathode reaction layer $\sigma_{ioCRL}$ (S m$^{-1}$) | $(1 - \Phi_{CRL}) \left( \dfrac{1 - \varepsilon_{CRL}}{\tau_{tort,CRL}} \right) \sigma_{ioEL}$ | [18] |
| Electrical conductivity of cathode reaction layer $\sigma_{elCRL}$ (S m$^{-1}$) | $9.3 \times 10^3$ | [16,17] |
| Electrical conductivity of cathode diffusion layer $\sigma_{elCDL}$(S m$^{-1}$) | $1.52 \times 10^4$ | [16,17] |
| Electrical conductivity of interconnect $\sigma_{elIN}$ (S m$^{-1}$) | $1.13 \times 10^6$ | / |
| Contact angle between electron- and ion- conducting particles in reaction layer $\theta$(°) | 30 | [17] |
| Radius of electron-conduction particles $r_{el}$ (m) | $1.0 \times 10^{-7}$ | [20] |
| Radius of ion-conduction particles $r_{io}$ (m) | $1.0 \times 10^{-7}$ | [20] |
| Thermal conductivity of anode $\lambda_A$ (W m$^{-1}$ K$^{-1}$) | 6 | [20] |
| Thermal conductivity of electrolyte $\lambda_E$ (W m$^{-1}$ K$^{-1}$) | 2.7 | [17] |
| Thermal conductivity of cathode $\lambda_C$ (W m$^{-1}$ K$^{-1}$) | 11 | [17] |

(1) Momentum equations

In the air and fuel channels,

$$-\nabla \cdot [\mu(\nabla \mathbf{u} + (\nabla \mathbf{u})^T)] + \rho(\mathbf{u} \cdot \nabla)\mathbf{u} + \nabla p = 0 \qquad (6)$$

In the porous electrodes, the Brinkman equation is adopted,

$$\left( \frac{\mu}{\kappa} + S_m \right) \mathbf{u} = \frac{1}{\varepsilon} \nabla \cdot [\mu(\nabla \mathbf{u} + (\nabla \mathbf{u})^T)] - \nabla p \qquad (7)$$

where $\mu$ is the dynamic viscosity of the gas mixture; $\kappa$ the permeability of the porous media; $\varepsilon$ the porosity of the porous media; $S_m$ the source term of continuity.

The inlet condition for air and fuel is as follows

$$\mathbf{u} = U_0 \cdot \mathbf{n} \qquad (8)$$

The outlet boundary condition for air and fuel is set as a pressure outlet.

$$p = p_0 \qquad (9)$$

(2) Mass transfer equation

The Maxwell-Stefan equation involving Knudsen diffusion is used,

$$\nabla \left( -\rho \omega_i \sum D_{ij}^{eff} \left( \nabla x_i + (x_i - \omega_i) \frac{\nabla p}{p} \right) + \rho \omega_i \mathbf{u} \right) = S_i \qquad (10)$$

where $\rho$ denotes the density (kg/m$^3$), $\omega_i$ mass fraction of species $i$, $x_j$ the molar fraction of species $j$, $\mathbf{u}$ the velocity vector (m/s), $p$ the pressure (Pa). $D_{ij}^{eff}$ is an effective diffusion coefficient, which is calculated as follows [22,23],

$$D_{ij}^{eff} = \frac{\varepsilon}{\tau} \left( \frac{1}{D_{ij}} + \frac{1}{D_{iK}} \right)^{-1} \qquad (11)$$

where $D_{ij}$ is the binary diffusion coefficient and $D_{iK}$ denotes Knudsen coefficient for the species $i$.

The source term $S_i$ denotes the production or consumption of the species $i$ due to electrochemical reactions, which can be expressed as:

In the cathode reaction layer,

$$S_{O_2} = -\frac{J M_{O_2}}{4F} \qquad (12)$$

In the anode reaction layer,

$$S_{H_2} = -\frac{J M_{H_2}}{2F}, S_{H_2O} = \frac{J M_{H_2O}}{2F} \qquad (13)$$

The inlet mass fraction for air and fuel is specified.

$$\omega_i = \omega_{i,0} \qquad (14)$$

At the outlet, the convection is the dominating process to force the mass flow through the channel exits, and the mass flux due to the mass diffusion across the outlet is zero. The following condition is applied to all species.

$$\mathbf{n} \cdot \left( -\rho \omega_i \sum D_{ij}^{eff} \left( \nabla x_i + (x_i - \omega_i) \frac{\nabla p}{p} \right) \right) = 0 \qquad (15)$$

(3) Charge transfer equations

Conservation of electronic charge transfer reads,

$$\nabla \cdot (-\sigma_{el} \nabla \varphi_{el}) = S_{el} \tag{16}$$

Conservation of ionic charge transfer is,

$$\nabla \cdot (-\sigma_{io} \nabla \varphi_{io}) = S_{io} \tag{17}$$

In the cathode reaction layer,

$$S_{el} = -S_{io} = J \tag{18}$$

In the anode reaction layer,

$$S_{el} = -S_{io} = -J \tag{19}$$

In the electrolyte layer,

$$S_{io} = 0 \tag{20}$$

The boundary conditions for the charge transfer are outlined as below. As shown in Fig. 1(b), the electric ground for Eq. (16) is set at the top wall,

$$\varphi_{el} = 0 \tag{21}$$

For boundary 30 shown in Fig. 1(b), the operating voltage $V_{cell}$ is specified

$$\varphi_{el} = V_{cell} \tag{22}$$

The remaining boundaries for electronic and ionic transport are set as an insulation condition,

$$\mathbf{n} \cdot (-\sigma \nabla \varphi) = 0 \tag{23}$$

(4) Electrochemistry equations

The source term for Eqs. (16) and (17) can be acquired by Butler–Volmer equations as

$$J_{an} = A_v J_{0,ref}^{H_2} \left( \frac{c_{H_2}}{c_{H_2,ref}} \right)^{\gamma_{H_2}}$$
$$\times \left\{ \exp \left( \frac{\alpha n F \eta_{act,an}}{RT} \right) - \exp \left( -\frac{(1-\alpha)nF\eta_{act,an}}{RT} \right) \right\} \tag{24}$$

$$J_{ca} = A_v J_{0,ref}^{O_2} \left( \frac{c_{O_2}}{c_{O_2,ref}} \right)^{\gamma_{O_2}}$$
$$\times \left\{ \exp \left( \frac{\alpha n F \eta_{act,ca}}{RT} \right) - \exp \left( -\frac{(1-\alpha)nF\eta_{act,ca}}{RT} \right) \right\} \tag{25}$$

where $A_v$ is the actual reactive surface area per unit volume, $J_{0,ref}^{H_2}$ and $J_{0,ref}^{O_2}$ are the reference exchange current densities for $H_2$ oxidation and $O_2$ reduction reactions at the reference concentrations, $c_{H_2,ref}$ and $c_{O_2,ref}$, respectively, and $\alpha$ is the charge transfer coefficient (or symmetry factor), whose value lies between zero and unity, $n$ the number of electrons participating in the electrochemical reactions and $\eta_{act}$ the electrode activation overpotential (anode or cathode), defined as [24]

$$\eta_{act,an} = V_{rev,an} - \left| \varphi_{el} - \varphi_{io} \right| \tag{26}$$

$$\eta_{act,ca} = V_{rev,ca} - \left| \varphi_{el} - \varphi_{io} \right| \tag{27}$$

As stated in Ref. [25], the values of $c_{H_2,ref}$ and $c_{O_2,ref}$ are 10.78 mol m$^{-3}$ and 2.38 mol m$^{-3}$, and the corresponding values of the reference exchange current densities, $J_{0,ref}^{H_2}$ and $J_{0,ref}^{O_2}$, are 1320 (A m$^{-2}$) and 400 (A m$^{-2}$), respectively. In order to enhance the predictive capability of the model, the expression used to model the reactive surface area per unit volume is based on random packing of binary spherical particles developed by Costamagna et al. [26]. This is given as

$$A_v = \pi \sin^2 \theta r_{el}^2 n_t n_{el} n_{io} \frac{Z_{el} Z_{io}}{Z} p_{el} p_{io} \tag{28}$$

where $\theta$ is the contact angle between the electron- and ion-conducting (Ni and YSZ) particles in the reaction zone layers, $r_{el}$ the radius of the electron-conducting (Ni) particles, $n_t$ the total number of particles per unit volume, $n_{el}$ and $n_{io}$ are the number fractions of the electron- and ion-conducting particles in the reaction zone layers, respectively. $Z_{el}$ and $Z_{io}$ are the coordination numbers of the electron- and ion-conducting particles in the reaction zone layers, respectively, $Z$ is the total average number of contacts of each particle, $p_{el}$ and $p_{io}$ are the probabilities of the electron- and ion-conducting particles in the reaction zone layers, respectively. The detailed discussion on the above mentioned parameters can be found in, e.g., Refs. [25,26,18].

(5) Energy equation

The local thermal equilibrium assumption is adopted in the heat transfer model.

$$\nabla \cdot (-\lambda \nabla T) = S_q - \rho C_P \mathbf{u} \cdot \nabla T \tag{29}$$

The equation is applied for the whole domain, but the convection term is considered only for the fuel and oxidant channels, and omitted in the porous electrode for the velocity in the electrodes is quite small. The source term $S_q$ in Eq. (29) is formulated as:

in the interconnect and anode/cathode diffusion layer,

$$S_q = \sigma_{el} \nabla \varphi_{el} \cdot \nabla \varphi_{el} \tag{30}$$

in the electrolyte,

$$S_q = \sigma_{io} \nabla \varphi_{io} \cdot \nabla \varphi_{io} \tag{31}$$

in the anode/cathode reaction layer,

$$S_q = \sigma_{el} \nabla \varphi_{el} \cdot \nabla \varphi_{el} + \sigma_{io} \nabla \varphi_{io} \cdot \nabla \varphi_{io} - \frac{J}{2F} T \Delta S - J \eta_{act} \tag{32}$$

For the inlet, the temperature of air and fuel is given as

$$T = T_0 \tag{33}$$

For the outlet, only the convective heat tranfer is considered and local one-way flow is assumed.

$$\mathbf{q} = \mathbf{n} \cdot (\rho C_p \mathbf{u} T) \tag{34}$$

For the air and fuel channel walls, the net radiation heat flux $q_r$ is also included.

$$\mathbf{n} \cdot (-\lambda \nabla T) = h(T_w - T_f) + q_r \tag{35}$$

where the convective heat transfer coefficient $h$ is deduced from the Nusselt number which is recommended as 3.09 in Ref. [27].

$$h = \frac{Nu \lambda_{gas}}{D_h} \tag{36}$$

The hydraulic diameter is defined as,

$$D_h = \frac{2W_{CH} H_{CH}}{W_{CH} + H_{CH}} \tag{37}$$

### 2.2.3. Model validation

Before proceeding further, it is necessary to ascertain the reliability and accuracy of the present numerical model and the code developed. Grid independence tests are carried out under the condition of operating voltage 0.75 V, emissivity 0.5, and the cell length 0.02 m. A tetrahedral mesh is adopted. Fig. 2 shows the variation of the average outlet temperature of air with different numbers of grid points. When the grid mesh number changes from 38,700 to 103,200, the average outlet temperature of air changes from 1108.8 K to 1110.4 K (i.e., 0.14%). With the increase of the number of points, the increase rate of average outlet temperature decreases, and the average outlet temperature varies slightly when the number of grid points reaches 103,200, which
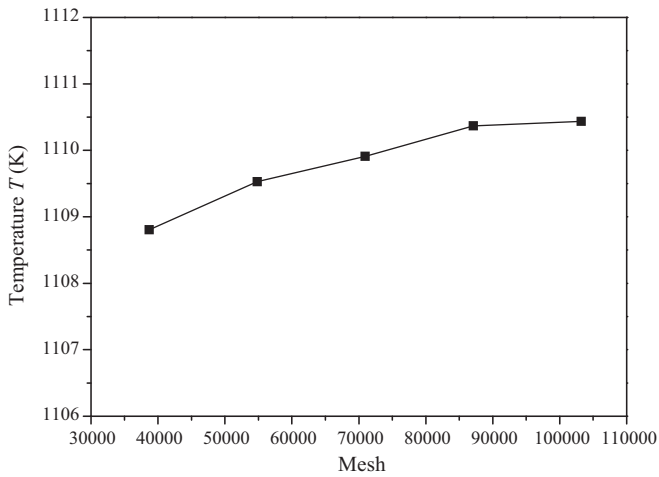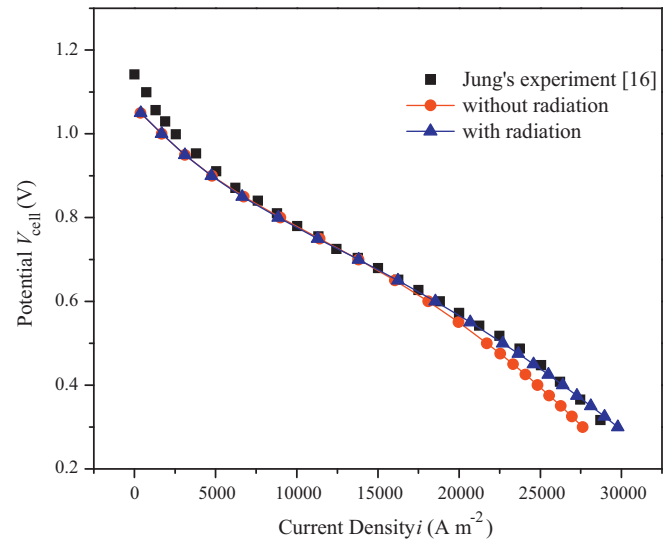
**Fig. 2.** Grid independence test.



**Fig. 3.** Model validation.

is used for taking both the accuracy and convergence rate into account.

In order to validate the present model, quantitative comparisons are also made with the cases investigated experimentally in [16], where the cell length is 5 cm. The comparison results with and without thermal radiation are shown in Fig. 3. In the radiation model, the emissivity is 0.5. When the current density is among 0–3000 A m$^{-2}$, the predictions by both models have a certain deviation from the experimental results. When the current density is greater than 3000 A m$^{-2}$, the numerical result with the radiation model agrees well with the experimental data. When the current density is greater than 15,000 A m$^{-2}$, the simulation result without radiation model deviates from the experimental data gradually. It is clear that the current density predicted by the model without radiation is smaller than the one with the radiation at the same voltage. This means that the model without thermal radiation underestimates the performance of SOFCs. This is so because with the increase of the current density, the cell average temperature and the temperature difference between the inlet and the outlet increase quickly, and radiative heat transfer becomes increasingly significant, which leads to the difference in the calculation results. The comparison result illuminates that present model with thermal radiation is convincing.

## 3. Results and discussion

### 3.1. Influence of emissivity on SOFC performance

The emissivity of a surface represents the ratio of the radiation emitted by the real surface to that emitted by a blackbody at the same temperature. Emissivity is a measure of how closely a real surface approximates a blackbody. The emissivity of a real surface is not a constant. Rather, it varies with the temperature of the surface as well as the wavelength and the direction of the radiation [21]. A brief survey of the literature reveals that the thermal radiative properties of the materials used in a SOFC are not easy to find at their operating temperatures [2], and it is difficult to describe the emissivity of the channel and electrode surfaces exactly. In the present study, the same emissivity of the channel and electrode surfaces is employed similar to what was adopted in [4].

Figs. 4 and 5 show the local temperature distribution for the cross-section at the positions close to the inlet and outlet, in which the maximum and minimum temperatures are indicated. Table 4 lists the average wall temperature in the air channel and the maximum and minimum temperatures for the cross-section at the positions close to the inlet and outlet. In Fig. 4 and Table 4, it is found

**Table 4**
Effect of emissivity on the average temperature in different x plane (Unit: K).

| | $\varepsilon$ | Temperature at top and bottom air channel walls | | | The maximum and minimum temperature in cross section | | |
|---|---|---|---|---|---|---|---|
| | | $T_{\text{wall-23}}$ | $T_{\text{wall-27}}$ | $\Delta T = T_{\text{wall-23}} - T_{\text{wall-27}}$ | $T_{\min}$ | $T_{\max}$ | $\Delta T = T_{\max} - T_{\min}$ |
| | 0.00 | 1086.60 | 1086.00 | 0.60 | 1085.36 | 1086.71 | 1.35 |
| | 0.05 | 1085.26 | 1084.66 | 0.60 | 1084.11 | 1085.38 | 1.27 |
| | 0.10 | 1085.01 | 1084.41 | 0.60 | 1083.88 | 1085.12 | 1.24 |
| | 0.20 | 1084.75 | 1084.16 | 0.59 | 1083.64 | 1084.87 | 1.23 |
| $x = 0.002$ m | 0.40 | 1084.51 | 1083.92 | 0.59 | 1083.42 | 1084.63 | 1.21 |
| | 0.60 | 1084.38 | 1083.79 | 0.59 | 1083.30 | 1084.49 | 1.19 |
| | 0.80 | 1084.28 | 1083.71 | 0.57 | 1083.21 | 1084.40 | 1.19 |
| | 1.00 | 1084.21 | 1083.65 | 0.56 | 1083.15 | 1084.32 | 1.18 |
| | 0.00 | 1124.06 | 1123.42 | 0.64 | 1122.95 | 1124.19 | 1.24 |
| | 0.05 | 1116.63 | 1116.02 | 0.61 | 1115.57 | 1116.76 | 1.19 |
| | 0.10 | 1114.89 | 1114.29 | 0.60 | 1113.84 | 1115.01 | 1.17 |
| | 0.20 | 1113.18 | 1112.59 | 0.59 | 1112.14 | 1113.30 | 1.16 |
| $x = 0.018$ m | 0.40 | 1111.57 | 1110.99 | 0.58 | 1110.53 | 1111.69 | 1.16 |
| | 0.60 | 1110.69 | 1110.13 | 0.56 | 1109.66 | 1110.81 | 1.15 |
| | 0.80 | 1110.11 | 1109.55 | 0.56 | 1109.08 | 1110.23 | 1.15 |
| | 1.00 | 1109.68 | 1109.13 | 0.55 | 1108.65 | 1109.79 | 1.14 |

(a) $\varepsilon=0$ ,(b) $\varepsilon=0.2$,(c) $\varepsilon=0.6$,(d) $\varepsilon=1.0$
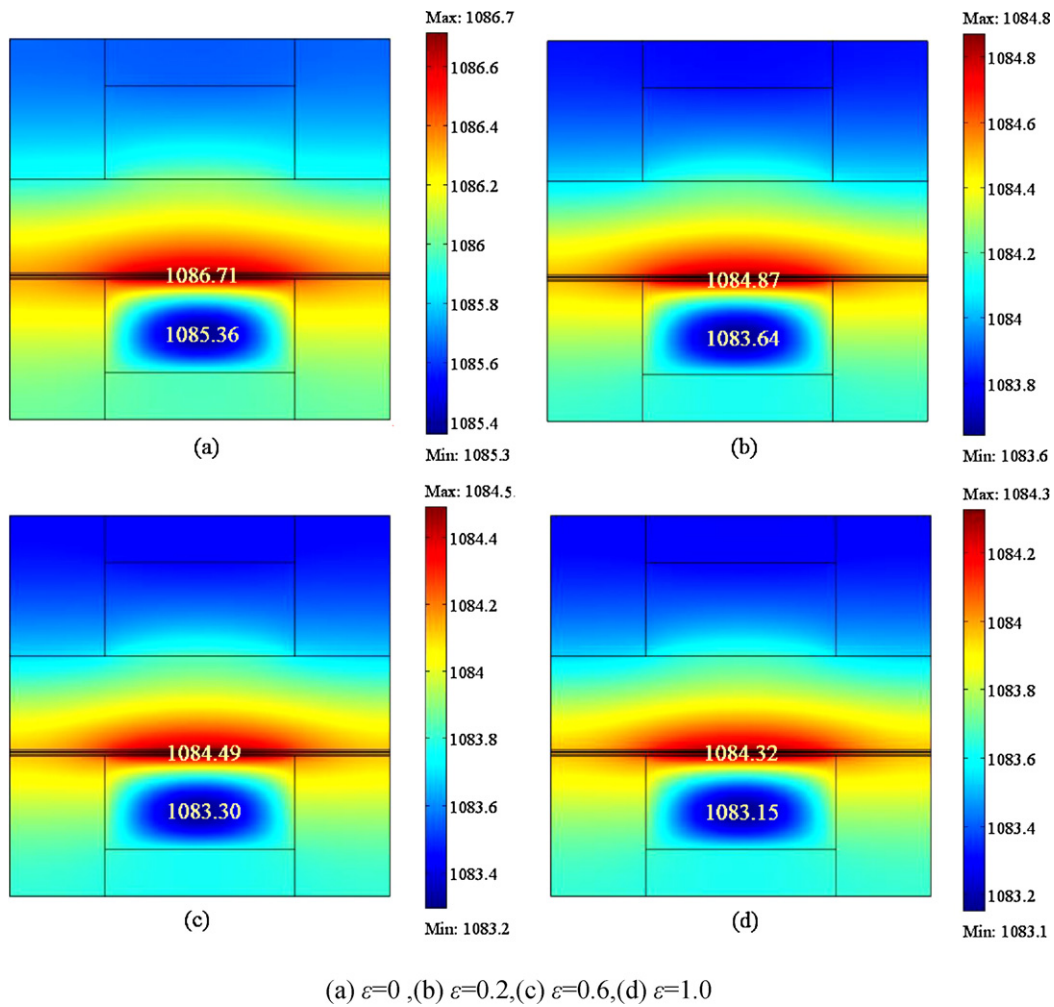
**Fig. 4.** Local temperature distribution in the plane of $x = 0.002$ m (close to the intlet, Co-flow, unit: K).

that the temperature distribution profiles are almost the same for the cases without and with radiation, e.g., the maximum temperature appears near the electrolyte and the minimum one in the middle region of the air channel. With the increase of emissivity, the maximum and minimum temperatures decrease slightly, as shown in Fig. 4(b–d), and the temperature difference between the maximum and minimum temperature decreases as well (Table 4). On the other hand, the temperaure difference between the top wall and the bottom wall in the cathode is almost the same. As for the postion close to the outlet shown in Fig. 5 and Table 4, the lowest temperature appears in the anode side instead, and both the maximum and minimum temperatures are higher. It is also clear that there is a great difference in temperatures for the cases without (Fig. 5(a)) and with radiation (Figs. 5(b–d)). However, the temperature difference between the walls is roughly the same (0.6 K), and the variation of the difference between the highest and the lowest temperatures is kept almost similar for the specific cases studied. Fig. 6 shows the local temperature distribution at the same operating voltage ($V_{cell}=0.75$ V). The trends of the local temperature distribution for all the cases are similar, i.e., the local temperature increases along the main flow direction due to the exothermic electrochemical reaction. However, with the increase of emissivity, the local temperature decreases, which leads to a decrease in the local current density compared to the case without radiation, as shown in Fig. 7. When the temperature is low, the rate of electrochemical reactions in the reaction layer becomes small, and the current density decreases at the same time. For the positions between

$x = 0.015$ m and 0.02 m, the local current density decreases with the increase of temperature. This is mainly due to the lower mole fraction of hydrogen and oxygen due to the gradual consumption of hydrogen and oxygen by the electrochemical reactions.

As is known to all, the average current density directly characterizes the overall cell performance. When the operating voltage is kept constant, the average power density can be acquired by the production of average current density and operating voltage. Fig. 8 shows the effects of emissivity on the average current density for a co-flow channel arrangement at $V_{cell}=0.75$ V. When the emissivity increases from 0 to 0.2, the average current density decreases rapidly, and with the further increase in emissivity, the average current density reduces gradually. For SOFCs, the surface emissivity between 0.3 and 1 is generally adopted by various researchers [28–31]. However, from Fig. 8 it is found that the emissivity variation between 0.3 and 1 has a small influence on the current density. It is clear that the numerical results rely mainly on how big the emissivity is.

To account for the effects of emissivity on the cell electrochemical performance, a relative current density at the same operating voltage is defined as

$$i' = \frac{\text{Current density with non-zero emissivity}}{\text{Current density with zero emissivity}} \quad (38)$$

with which, one can compare the magnitude of the impact of the emissivity on the average current density at different operating voltage. Fig. 9 gives the variation of the relative current density
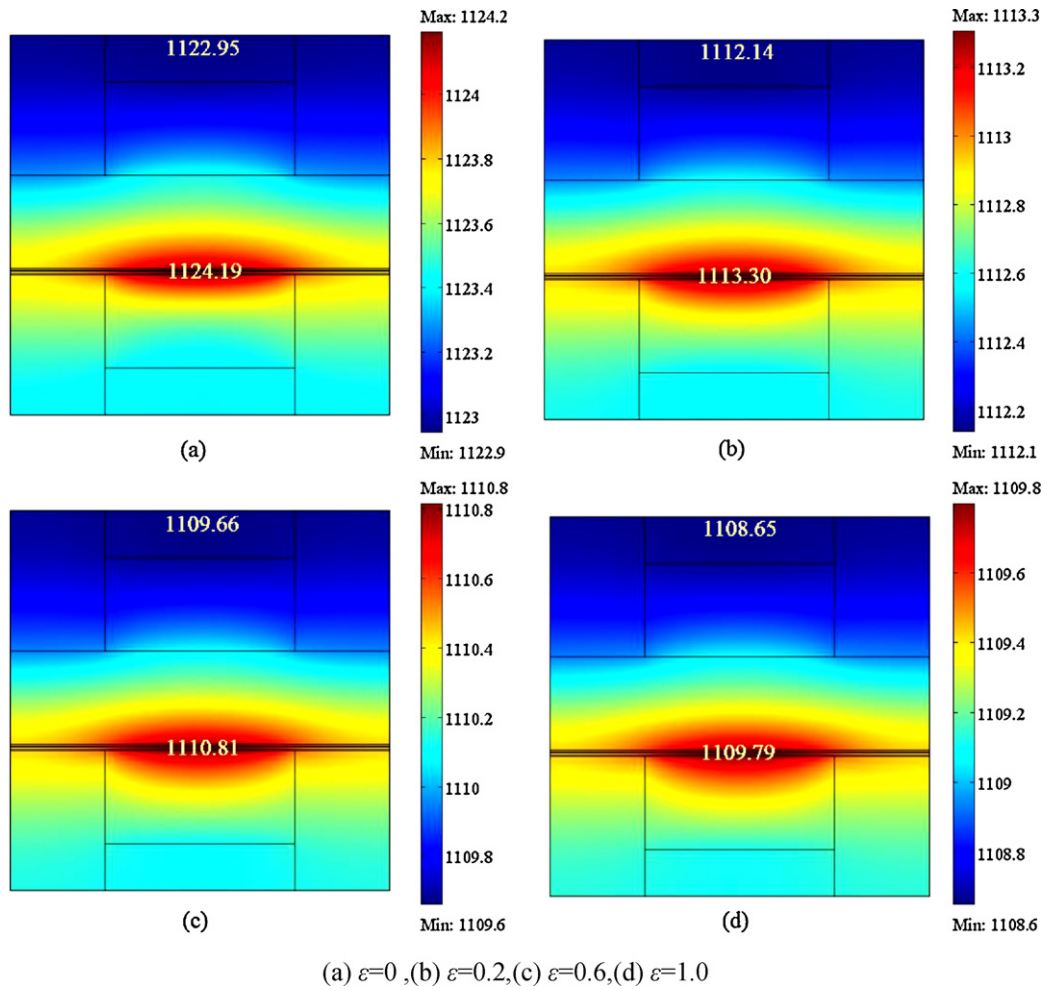
(a) $\varepsilon=0$ ,(b) $\varepsilon=0.2$,(c) $\varepsilon=0.6$,(d) $\varepsilon=1.0$

**Fig. 5.** Local temperature distribution in the plane of $x = 0.018$ m (close to the outlet, Co-flow, unit: K).

with emissivity for the voltages 0.55 V, 0.75 V and 0.85 V. The trend for the three cases is the same, i.e., the relative current density decreases quickly when the emissivity is between 0 and 0.2, and after that it varies smoothly. When the operating voltage decreases, the average current density and the heat generation will increase. The lower the operating voltage, the greater is the impact of thermal radiation. However, variation of the current density leads to a variation of ohmic heat generation, which will affect the average temperature of the cell. This once again illustrates that the lower the operating voltage, the greater the impact of the emissivity on the average temperature of cell. This is confirmed by Fig. 10. In addition, the net radiative heat flux is affected by
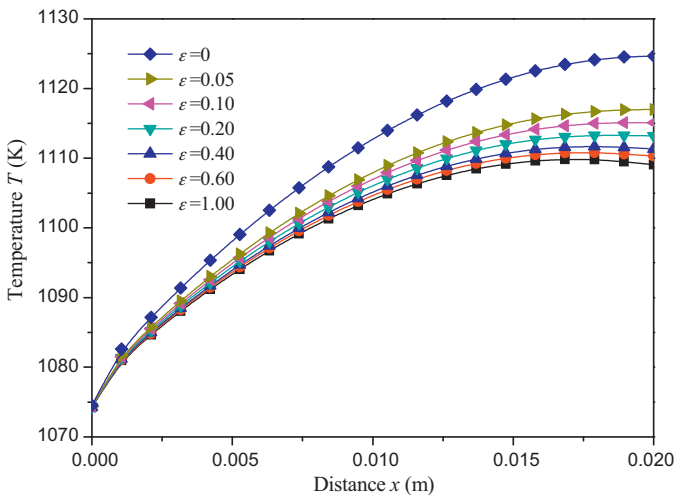


**Fig. 6.** Effect of the emissivity on the axial temperature distribution in electrolyte ($V_{cell} = 0.75$ V, Co-flow).
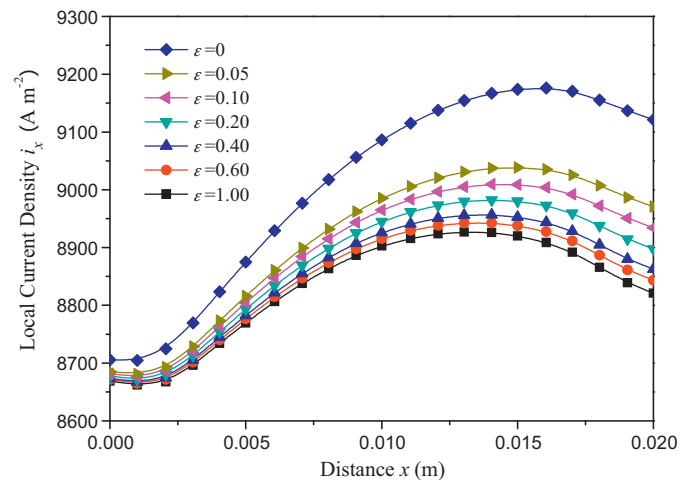


**Fig. 7.** Effect of the emissivity on the local current density distribution ($V_{cell} = 0.75$ V, Co-flow).
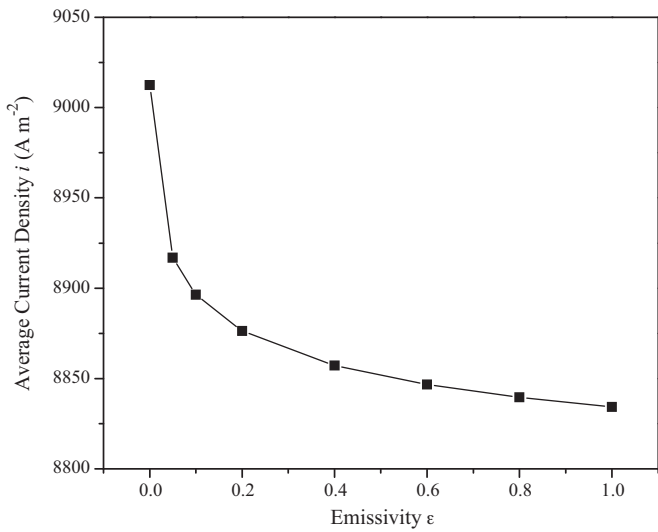
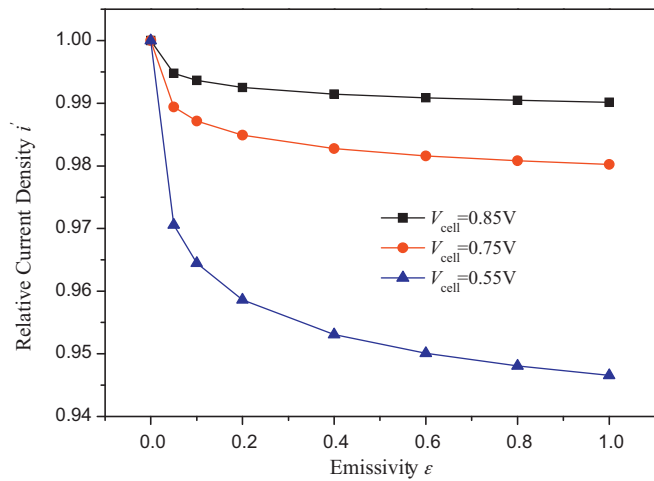**Fig. 8.** Effect of the emissivity on the average current density ($V_{cell}$ = 0.75 V, Co-flow).



**Fig. 9.** Effect of the emissivity on the relative current density under different operation voltage (Co-flow).

the cell temperature. Fig. 11 shows the effects of emissivity on the net radiative heat flux. It is found that the net radiative heat flux increases rapidly with the increase of emissivity at first. However, the increase of net radiative heat flux will lead to a decrease of
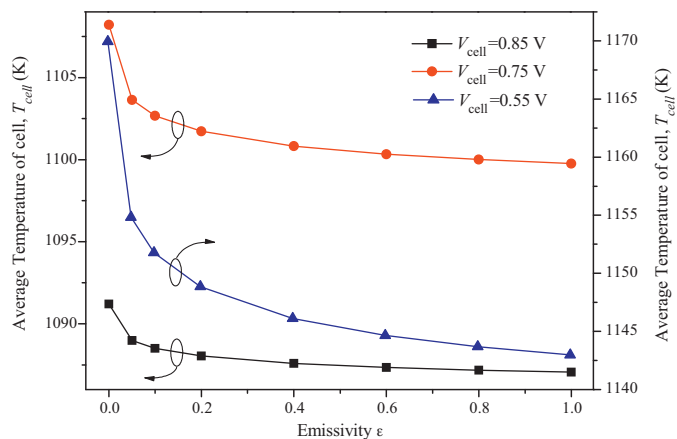


**Fig. 10.** Effect of the emissivity on the cell average temperature under different operation voltage (Co-flow).
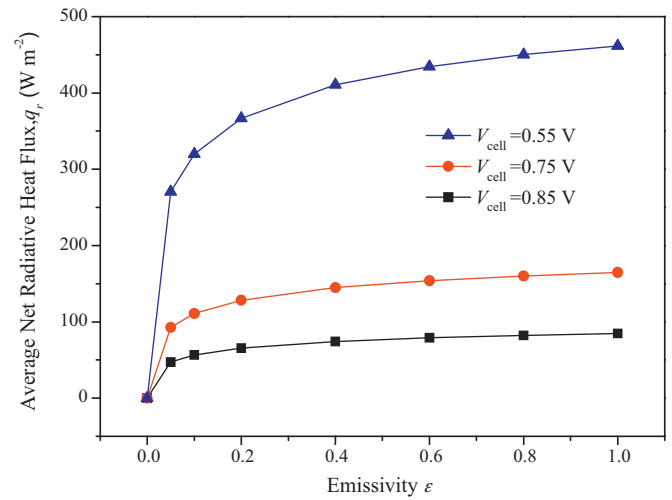


**Fig. 11.** Effect of the emissivity on the net radiation heat flux under different operation voltage (Co-flow).

the cell temperature, and in turn it reduces the net radiative heat flux. These interactions move back and forth, and ultimately a balance between temperature and net radiation heat flux might be achieved, which leads to a slight variation of the net radiation heat flux and cell temperature for a high emissivity.

### 3.2. Influence of ambient temperature on SOFC performance

Fig. 12 shows an interconnect unit adopted in the experiment work in [32]. The highlighted region is the single-cell channel, 2 and 3 are the inlet and outlet, respectively. The complete radiation model should consider the radiative heat transfer effects of the components 1 and 4. However, the temperature of 1 and 4 is difficult to obtain from the single-cell model, and must be solved through the cell-stack model. The temperatures of 1 and 4 might be maintained at a certain value if a suitable thermal management is adopted for instance, they can be treated as the environmental temperature. In Section 3.1, the ambient temperature is set equal to inlet temperature of the fuel, and effects of different ambient temperature on cell performance will be discussed in this Section. Five cases with the ambient temperature 973 K, 1023 K, 1073 K, 1123 K and 1173 K are investigated separately.
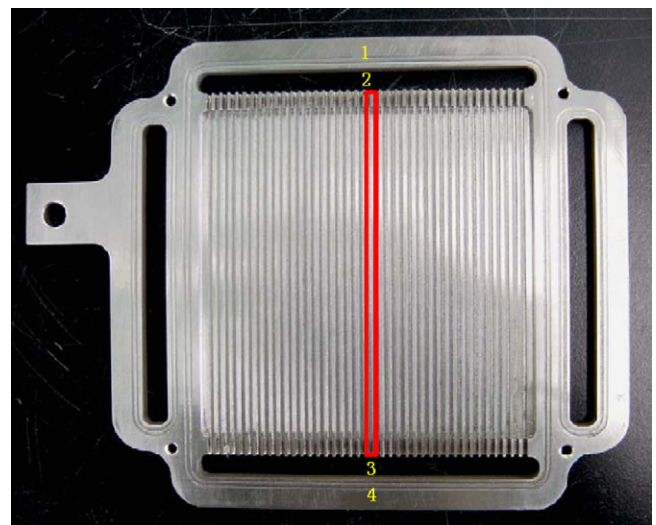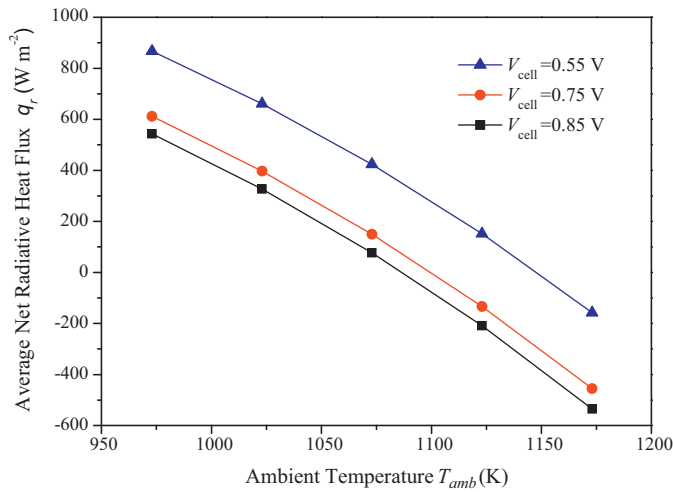


**Fig. 12.** Interconnet unit in Ref. [32].

**Fig. 13.** Effect of the ambient temperature on the average net radiation heat flux ($\varepsilon = 0.5$).

The effects of the ambient temperature on the average net radiation heat flux are shown in Fig. 13. When the ambient temperature is low, the average net radiation heat flux is positive, which means that the radiation heat transfer rate from the stack to the ambient is greater than that from ambient to the stack. With the increase of ambient temperature, the radiative heat transfer flux from the ambient to the cell increases, and finally it exceeds that from the stack to the ambient, which leads to a negative net radiation heat flux. In addition, at a constant ambient temperature, a lower operating voltage results in a greater net radiation heat flux. Fig. 14 reveals the effects of ambient temperature on the average cell temperature. It is found that the average cell temperature increases with increasing ambient temperature. When the operating voltage is kept constant (0.55 V, 0.75 V and 0.85 V), the relative average cell temperature for $T_{amb} = 1173$ K increases about 2.83%, 2.80% and 2.78%, or 32.1 K, 30.5 K and 29.8 K, respectively, compared to those predicted for $T_{amb} = 973$ K. This finding reveals that, with increasing ambient temperature, the operating voltage has a small influence on the average cell temperature. The effect of ambient temperature on the average current density is illustrated in Fig. 15. It is found that increasing the ambient temperature has a small effect on the average current density.
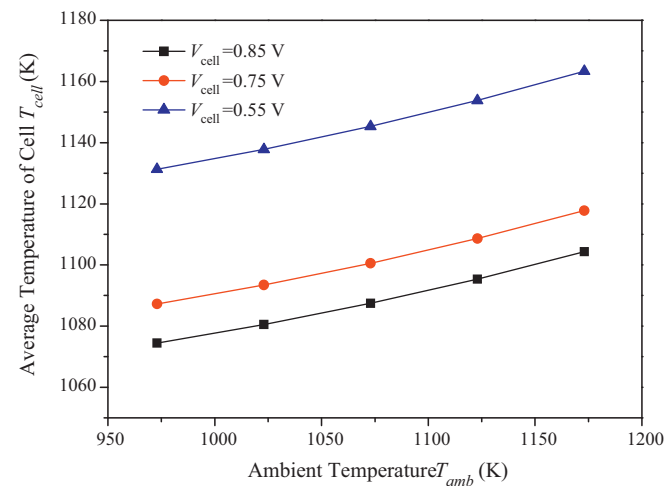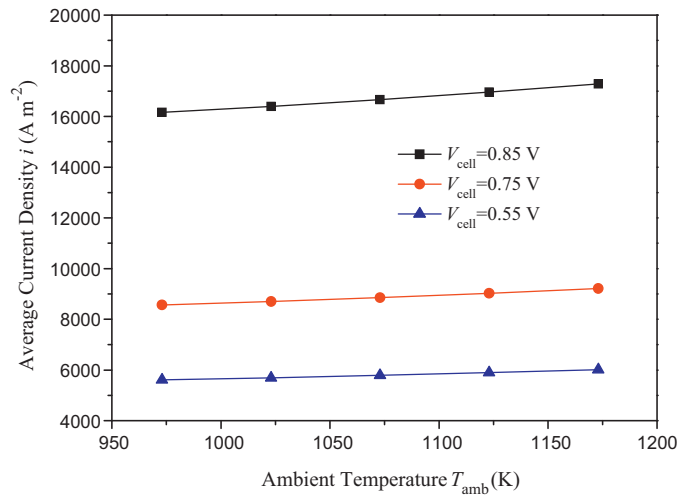


**Fig. 15.** Effect of ambient temperature on the average current density ($\varepsilon = 0.5$).

### 3.3. Influence of flow pattern on SOFC performance

In the above discussed sections, the focus is on the performance of SOFC under the co-flow condition. Planar stacks can be characterized according to arrangement of the gas flow: Co-flow (air and fuel flow in parallel and in the same direction), counter-flow (in parallel but in opposite direction) and cross-flow (perpendicular to each other). There is a great difference among the three flow arrangements. Only the counter-flow and the co-flow configurations are considered in this study because numerous meshes are necessary to model the cross-flow pattern case and the calculation time becomes very long.

At the same operating voltage, the effects of emissivity on the average current density for different flow arrangement are shown in Fig. 16. The variation of the current density for the counter-flow shows the same trend as that of co-flow, i.e., there is a rapid change in the current density when the emissivity is small, and the variation tends to be flat when the emissivity is big. Overall, the change in counter-flow is smaller than that in co-flow because the two flow arrangements have different local temperature distribution. Fig. 17 shows the local temperature distribution in the air channel. For the co-flow, the maximum temperature occurs in the outlet region. For the counter-flow, a constant temperature is set at the
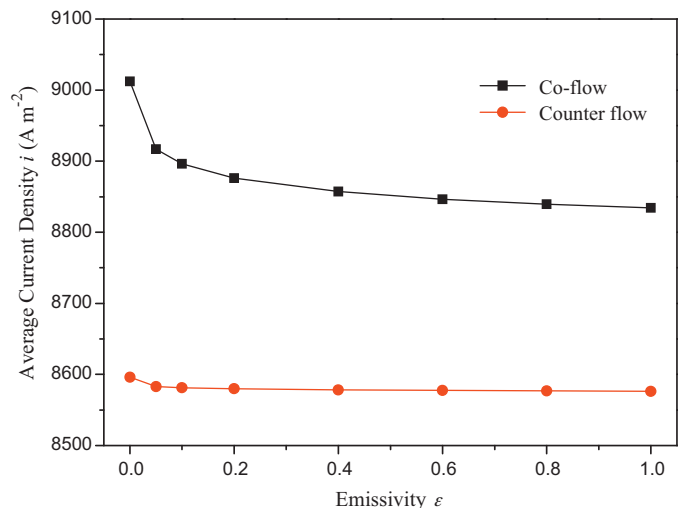


**Fig. 14.** Effect of the ambient temperature on the average temperature of cell ($\varepsilon = 0.5$).



**Fig. 16.** Effect of the emissivity on the average current density under different flow arrangement ($V_{cell} = 0.75$ V).

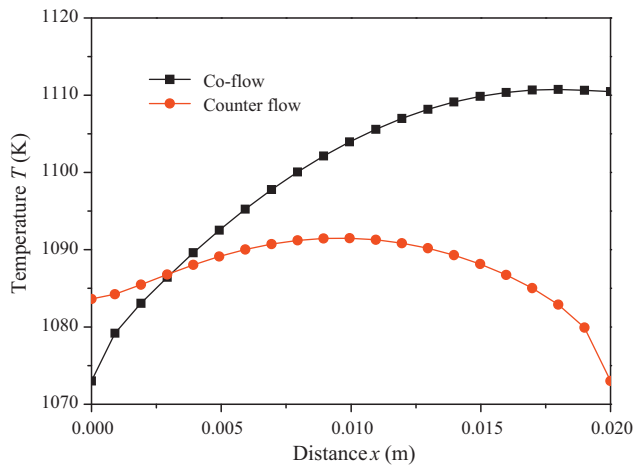**Fig. 17.** Local temperature distribution in air channel under different flow arrangement ($V_{cell}$ = 0.75 V, $\varepsilon$ = 0.5).
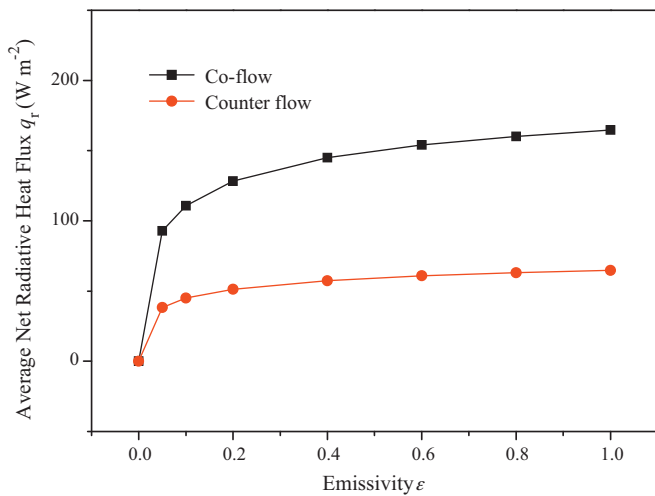


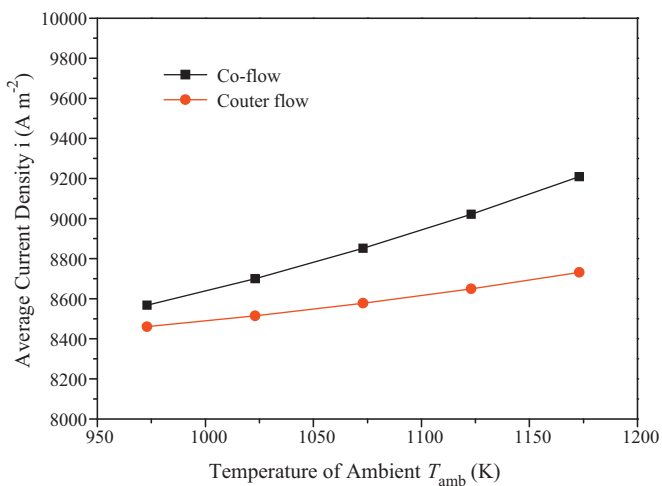**Fig. 18.** Effect of the emissivity on the net radiation heat flux under different flow arrangement ($V_{cell}$ = 0.75 V).



**Fig. 19.** Effect of the ambient temperature on the average current density under different flow arrangement ($V_{cell}$ = 0.75 V, $\varepsilon$ = 0.5).

inlets of air and fuel, which leads to a maximum temperature in the middle part of the cell. Because the view factors between the ambient and surfaces near the inlet and the outlet are much bigger, the corresponding radiative heat transfer is also greater. On the other hand, the radiative heat transfer between the ambient and the surface near the middle part of the cell is lower. Considering the maximum temperatures for the co-flow and the counter-flow, it is clearly found that the emissivity has less influence on the current density for counter-flow arrangement. The effects of emissivity on the net radiation heat flux for different flow arrangement are shown in Fig. 18. The emissivity also has less influence on the average net radiation heat flux for counter-flow arrangement.

Fig. 19 shows the effect of the ambient temperature on the current density. At the same operating voltage, the ambient temperature has less influence on the current density for the counter-flow, compared to the co-flow arrangement.

## 4. Conclusions

To investigate radiative heat transfer, a 3D comprehensive model has been developed for calculation of the performance characteristics of planar solid oxide fuel cells. The effects of emissivity, ambient temperature and flow arrangement are investigated in details. The major findings are as follows.

(1) With the increase of emissivity, the current density decreases quickly at small $\varepsilon$ but only slightly at big $\varepsilon$, particularly at low operating voltage.
(2) For the typical materials for SOFC the emissivity is between 0.3 and 1, and it is found that the emissivity has a small influence on the simulation results when thermal radiation is considered.
(3) The effects of ambient temperature on the performance of SOFC are relatively small. With increasing ambient temperature, the average temperature and current density of the cell will increase, but the variation is small. In addition, the relative current density increases faster than the average temperature.
(4) For different flow arrangements, the radiation for co-flow has a bigger influence on the performance of SOFC than for counter-flow.

## References

[1] Fuel Cell Handbook, seventh ed., EG&G Services, National Technical Information Service, U.S. Department of Commerce, 2004.
[2] B. Rousseau, H. Gomart, D.S.M. Domingos, E. Patrick, R. Mathilde, D. Romain, L. Pascal, J. Electroceram. 27 (2) (2011) 89–92.
[3] H. Karoliussen, K. Nisancioglu, A. Solheim, J. Appl. Electrochem. 28 (3) (1998) 283–288.
[4] S. Murthy, A.G. Fedorov, J. Power Sources 124 (2) (2003) 453–458.
[5] G. Brus, J.S. Szmyd, J. Power Sources 181 (1) (2008) 8–16.
[6] D.L. Damm, A.G. Fedorov, J. Fuel Cell Sci. Technol. 2 (4) (2005) 258–262.
[7] D.L. Damm, A.G. Fedorov, J. Power Sources 143 (1–2) (2005) 158–165.
[8] K.J. Daun, S.B. Beale, F. Liu, J. Power Sources 157 (1) (2006) 302–310.
[9] J.D.J. VanderSteen, J.G. Pharoah, J. Fuel Cell Sci. Technol. 3 (1) (2006) 62–67.
[10] D. Sanchez, R. Chacartegui, A. Munoz, J. Power Sources 160 (2) (2006) 1074–1087.
[11] H. Yakabe, T. Ogiwara, M. Hishinuma, I. Yasuda, J. Power Sources 102 (1–2) (2001) 144–154.
[12] R.J. Kee, B.L. Kee, J.L. Martin, J. Power Sources 195 (19) (2010) 6688–6698.
[13] M. García-Camprubí, H. Jasak, N. Fueyo, J. Power Sources 196 (17) (2011) 7290–7301.
[14] C. Bao, N. Cai, E. Croiset, J. Power Sources 196 (6) (2011) 3223–3232.

[15] T.X. Ho, P. Kosinski, A.C. Hoffmann, Int. J. Hydrogen Energy 35 (9) (2010) 4276–4284.
[16] H.Y. Jung, W.S. Kim, S.H. Choi, H.C. Kim, J. Kim, H.W. Lee, J.H. Lee, J. Power Sources 155 (2) (2006) 145–151.
[17] D.H. Jeon, Electrochim. Acta 54 (10) (2009) 2727–2736.
[18] M.M. Hussain, X. Li, I. Dincer, J. Power Sources 189 (2) (2009) 916–928.
[19] J.R. Ferguson, J.M. Fiard, R. Herbin, J. Power Sources 58 (2) (1996) 109–122.
[20] S. Sunde, J. Electroceram. 5 (2) (2000) 153–182.
[21] A.C. Yunus, Heat Transfer—A Pratical Approach, 2nd ed., McGraw-Hill Companies, Inc., New York, 2003.
[22] Q.Y. Chen, M. Zeng, J. Zhang, Q.W. Wang, Int. J. Hydrogen Energy 35 (9) (2010) 4292–4300.
[23] Q.Y. Chen, Q.W. Wang, J. Zhang, J.L. Yuan, Int. J. Heat Mass Transfer 54 (9–10) (2011) 1994–2003.
[24] R. Bove, S. Ubertini, Modeling Solid Oxide Fuel Cells: Methods, Procedures and Techniques, Springer, Netherlands, 2008, pp. 51–93.
[25] M.M. Hussain, X. Li, I. Dincer, J. Power Sources 161 (2) (2006) 1012–1022.
[26] P. Costamagna, P. Costa, V. Antonucci, Electrochim. Acta 43 (3–4) (1998) 375–394.
[27] P. Iora, P. Aguiar, C.S. Adjiman, N.P. Brandon, Chem. Eng. Sci. 60 (11) (2005) 2963–2975.
[28] P. Aguiar, D. Chadwick, L. Kershenbaum, Chem. Eng. Sci. 57 (10) (2002) 1665–1677.
[29] C. Stiller, B. Thorud, S. Seljebo, M. Oistein, K. Havard, B. Olaav, J. Power Sources 141 (2) (2005) 227–240.
[30] F. Calise, M.D. d'Accadia, G. Restuccia, Int. J. Hydrogen Energy 32 (17) (2007) 4575–4590.
[31] T. Shimada, T. Kato, Y. Tanaka, J. Fuel Cell Sci. Technol. 4 (3) (2007) 299–307.
[32] H.Y. Jung, S.H. Choi, H. Kim, J.W. Son, J. Kim, H.W. Lee, J.H. Lee, J. Power Sources 159 (1) (2006) 478–483.